RSC Advances

PAPER

View Article Online
View Journal | View Issue

Cite this: *RSC Adv.*, 2022, **12**, 25487

# Azo-functionalized superparamagnetic $Fe_3O_4$ nanoparticles: an efficient adsorbent for the removal of bromocresol green from contaminated water

Hadeel Saad,[ab] F. A. Nour El-Dien,*[a] Nadia E. A. El-Gamel[a] and Ahmed S. Abo Dena*[cd]

Water contamination is regarded as one of the world's worst tragedies owing to the continual depletion of water resources suitable for drinking and agriculture. Researchers have recently been interested in developing novel and more effective adsorbents for wastewater purification. We report herein a magnetic adsorbent nanomaterial for the removal of the anionic dye bromocresol green (BCG) from wastewater. The adsorbent is based on superparamagnetic iron oxide (cubic $Fe_3O_4$) nanoparticles (SPIONs) coated with a high-molecular-weight azo dye synthesized *via* diazo coupling of vitamin B1 with a trisubstituted benzene derivative. The proposed adsorbent was characterized using scanning electron microscopy, FTIR and $^1$H-NMR spectroscopy, mass spectrometry, dynamic light scattering, vibrating sample magnetometry, thermal analysis, and X-ray diffraction crystallography. At room temperature and pH 2.0, the synthesized adsorbent showed an average particle size of 65.9 ± 8.0 nm, a high magnetization saturation (65.58 emu $g^{-1}$), a high equilibrium adsorption capacity (36.91 mg $g^{-1}$). Adsorption of BCG was found to take place *via* a physisorption mechanism and followed a pseudo-second-order rate kinetics. Thermodynamic studies revealed that the adsorption process is enthalpy driven by hydrogen bonding and/or van der Waals interactions. After treating water samples with the suggested adsorbent, it can be easily removed from water using a strong external magnetic field.

Received 4th June 2022
Accepted 30th August 2022

DOI: 10.1039/d2ra03476j

rsc.li/rsc-advances

## Introduction

Recently, water pollution has captured researchers' attention due to its negative impact on plants, animals, and humans. One of the main emerging pollutants is synthetic dyes which often have complex chemical structures behind their mechanisms of action.[1] Synthetic and natural dyes have found vast applications in diverse industrial sectors, such as textiles, foods, chemicals, paints, and papers. The discharge of these dyes into water bodies constitutes one of the main environmental concerns.[2] Therefore, finding efficient water treatment methods to remove these hazardous contaminants from drinking water and wastewaters is highly required.[3]

Bromocresol green (BCG) is a synthetic dye that belongs to the triphenylmethane family. It is widely used in various applications, including but not limited to, textile industries, and is typically released in the aqueous effluents of factories, thus causing substantial environmental pollution.[3] The sodium salt of BCG is highly ionisable in water, and BCG itself has two possible forms in aqueous solutions based on the solution pH (the lactoid and quinoid forms). The lactoid (neutral) form is the predominant species in acidic solutions, while the quinoid (anionic) form dominates in alkaline media.[4] Plant powders,[5] activated carbon,[6] chitin nanofibers,[7] solvent sublation,[8] and electro-Fenton and electro-Fenton-like processes[9] are the methods reported in the literature for removing BCG from water. In one of our prior studies, BCG and another triphenylmethane dye (bromophenol blue) were removed from contaminated water by polyethyleneimine-coated $Fe_3O_4$ nanoparticles.[3]

Superparamagnetic iron oxide nanoparticles (SPIONs) are considered a versatile material in various applications such as drug delivery,[10–12] bio sensing,[13,14] water purification,[3,15] solid–phase extraction,[16,17] and even bio imaging.[18,19] SPIONs are known for their biosafety, easy functionalization, superparamagnetic properties, high stability, low cost, facile mass production, among other nanomaterials. On the other hand, azo dyes (ADs) are organic compounds obtained by a two-step synthesis process involving a diazotization step followed by a coupling step. This family of molecules possesses a characteristic chemical group that is able to form covalent bonds with

---

[a] Chemistry Department, Faculty of Science, Cairo University, Giza 12613, Egypt
[b] General Organization for Export and Import Control, Ramses Street, Cairo, Egypt
[c] Pharmaceutical Chemistry Department, National Organization for Drug Control and Research (NODCAR), Giza, Egypt. E-mail: ahmed_said5899@yahoo.com
[d] Faculty of Oral and Dental Medicine, Future University in Egypt (FUE), New Cairo, Egypt

various substrates.[20] The functionalization of different materials (*e.g.* metals, metal oxides, and polymers) with azo dyes has recently paved the way for a massive number of new applications, including the removal of pollutants from water.[10,21,22]

This study aims to synthesize azo-dye functionalized SPIONs (ADFS) for the adsorptive removal of BCG from aqueous solutions. To the best of our knowledge, this is the first azo-functionalized magnetic nanoparticles adsorbent in the literature to remove organic dyes from water.

The synthesized material has been characterized using the common nanomaterial characterization techniques such as FTIR spectroscopy, UV-vis spectrophotometry, Scanning Electron Microscope (SEM), Dynamic Light Scattering (DLS), Vibrating Sample Magnetometery (VSM), thermal analyses, Mass Spectrometry (MS), and $^1$H-NMR spectroscopy. After optimizing the adsorption conditions and investigating the removal kinetics and thermodynamics, the characterized materials were employed for the adsorptive removal of BCG from water samples.

## Materials and methods

### Materials

Bromocresol green (molecular formula: $C_{21}H_{14}Br_4O_5S$; CASN: 76-60-8; molar mass: 698.01 g mol$^{-1}$) was obtained from Carlo Erba Reagents (Barcelona, Spain). For the synthesis of the AD, thiamine hydrochloride (THC, molar mass of 337.27 g mol$^{-1}$, NODCAR, Egypt), also known as vitamin B1, tert-butyl-[2-(3,5-dihydroxyphenyl)2-hydroxyethyl]azanium sulphate (TBDA sulphate, molar mass of 548.65 g mol$^{-1}$, Borg Pharmaceutical Industries, Borg El-Arab, Alexandria, Egypt), sodium nitrite (SDFCL, India) and sodium carbonate (ADWIC, Egypt) were used. Ethylene glycol (Honeywell International Inc., USA), ferric chloride hexahydrate ($FeCl_3 \cdot 6H_2O$, Daejung Chemicals and Metals, South Korea) and anhydrous sodium acetate (ADWIC, Egypt) were used for the solvothermal synthesis of SPIONs. Ethyl alcohol was obtained from the International Company for Medical Industries (Egypt), and hydrochloric acid was purchased from Alpha Chemika (India). All reagents were of analytical grade and were used without any further purification. Throughout the experimental work, deionized water was used for preparing aqueous solutions. An aqueous 0.01 M stock solution of BCG was prepared by dissolving an appropriate quantity of BCG in the least amount of ethanol and then completing the volume with deionized water. Working solutions were prepared by subsequent dilution of the stock solution with deionized water.

### Instruments

The concentration of BCG was measured by a SPECORD250-PLUSAnalytikjena Spectrophotometer (Germany) by measuring the absorbance at 444 nm using a 1 cm quartz cell. A VEGA3 TESCAN field-emission scanning electron microscope (FESEM, Czech Republic) was used for studying particle size and surface morphology. The particle size and zeta potential (ZP) of naked SPIONs and ADFS materials were determined by DLS analysis using a Malvern Panalytical instrument (UK). Fourier transform infrared spectra (FTIR) were recorded using a Nicolet 6700 ATR-FTIR spectrometer (Thermo Scientific, Germany). The magnetic properties were investigated with a vibrating-sample magnetometer (VSM) (Lakeshore, model 7410). An X-ray diffraction (XRD) spectrometer (Discover-D8, Bruker, USA) was used to confirm the formation of the magnetite crystallographic structure. $^1$H-NMR spectra were recorded using a Varian 300 MHz NMR Spectrometer (Germany) using DMSO as a solvent. TGA and DTA analyses have been carried out using a Shimadzu 50 instrument. The mass spectrum of SMS was recorded using an LC-MS instrument (Thermo Scientific).

### Preparation of SPIONs

Superparamagnetic magnetite nanoparticles were synthesized by the modified solvothermal method in ethylene glycol.[3,15,23] Briefly, 2 g of $FeCl_3 \cdot 6H_2O$ and 6 g of anhydrous sodium acetate were dissolved in 65 mL of ethylene glycol. This mixture was transferred to a Teflon-lined solvothermal reactor and then heated to 200 °C in the oven (Heraeus, Thermo Electron Corporation, Germany) for 12 h. After the reaction, the solvothermal reactor was cooled to room temperature, and the formed black magnetite precipitate was collected with a strong magnet. Subsequently, the as-obtained product was washed several times using double distilled water and ethanol, and then dried at room temperature for 24 h.

### Preparation of ADFS

The ADFS was synthesized *via* a diazo-coupling reaction according to a reported procedure with minor modifications (Fig. 1).[24] Typically, 0.5 g of THC (1.5 mmol) and 1 g of SPIONs were added to 20 mL of concentrated HCl and stirred constantly at 4 °C for 20 min. Thereafter, 0.4 g of sodium nitrite (3 mmol) was dissolved in 5 mL of double distilled water and the resulting solution was slowly added to the above mixture in an ice bath with constant stirring. Then the pH of the mixture was neutralized by adding 50 mL of 0.5 M sodium carbonate. Finally, 0.3 g (*ca.* 1 mmol) of TBDA sulphate was dissolved in 5 mL of distilled water and dropped onto the mixture with constant stirring, and then the solution was continuously stirred for 12 h. The appearance of an orange precipitate indicates the formation of the ADFS. The obtained ADFS material was collected from the suspension with a strong magnet, and then washed generously with distilled water and dried overnight at room temperature.

### Adsorption experiments

Batch adsorption is a technique used for treating small volumes of the adsorbate in the laboratory. Batch studies were carried out to detect the pH, time, initial BCG concentration, adsorbent loading and temperature of maximum adsorption of BCG on ADFS.[25]

The pH of the dye solution was measured using a JENCO 6173 pH meter. Working solutions of pH 2–9, adjusted with the suitable buffer solution, were used to investigate the effect of pH on BCG adsorption. The exact pH values of these buffered

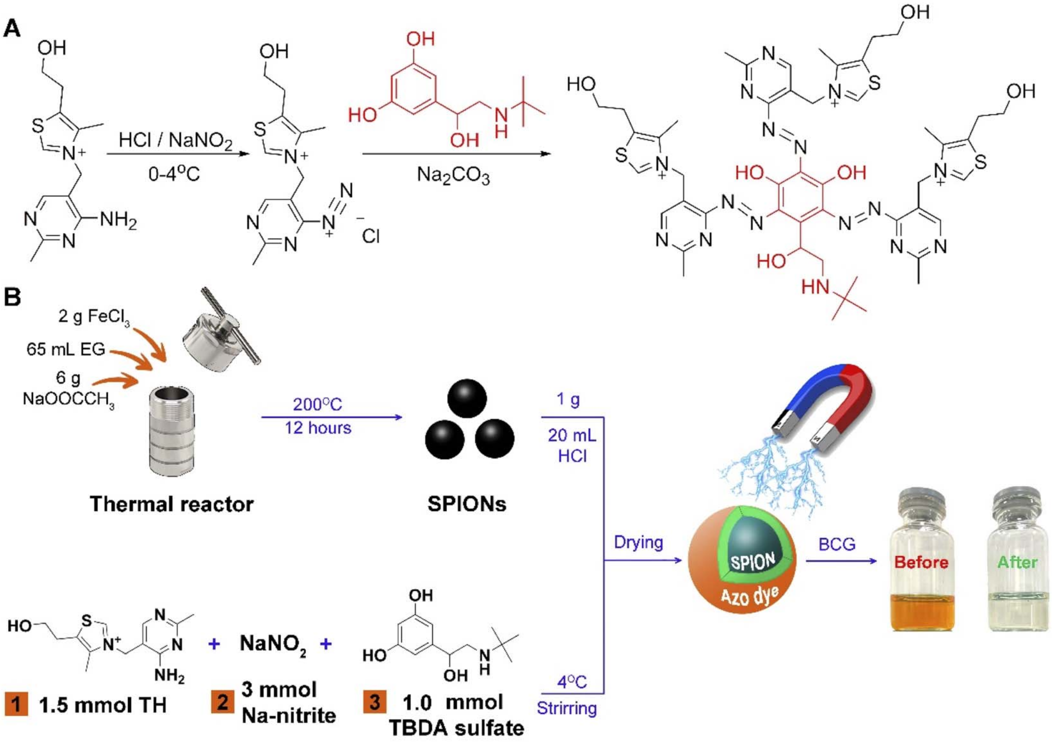

Fig. 1 Schematic diagram illustrating (A) the diazo-coupling reaction used to prepare the thiamine-based AD, and (B) the procedure of preparation of the proposed ADFS adsorbent.

solutions were adjusted by adding a few drops of 0.1 M NaOH or HCl solutions. A 10 mL aliquot of BCG solution of the appropriate concentration was shaken at 400 rpm in a temperature-controlled shaker adjusted to room temperature (Clifton, UK). After reaching the adsorption equilibrium, the adsorbent was separated by applying a strong external magnetic field. The remaining supernatant was filtered and the concentration of the residual (non-adsorbed) BCG was determined using a standard plot *via* measuring the absorbance at 444 nm.

The experiments for investigating the effects of contact time on the adsorption capacities of ADFS were carried out at varying incubation periods ranging from 10 min to 180 min at an adsorbent dose of 10 mg, room temperature (303 K), initial BCG concentration of 50 mg $L^{-1}$, and pH 2. Furthermore, the influence of the initial BCG concentration on the removal efficiency of ADFS was scrutinized in the range of 10–100 mg $L^{-1}$ at 10 mg of ADFS, pH 2, and 100 min contact time.

In order to study the influence of varying the adsorbent dose on BCG adsorption, at a BCG concentration of 100 mg $L^{-1}$, pH 2 and 100 min contact time, the various amounts of 5–300 mg of ADFS were selected. Finally, the effect of temperature on the adsorption of BCG on ADFS was investigated over the temperature range of 303–333 K using 100 mg $L^{-1}$ BCG solution, an adsorbent dose of 20 mg, pH 2, and a contact time of 100 min.

The percent removal of BCG was calculated from eqn (1).

$$\%\text{Removal} = \frac{(C_0 - C_e)}{C_0} \times 100 \tag{1}$$

where $C_0$ and $C_e$ are the initial and equilibrium concentrations of BCG in mg $L^{-1}$, respectively.

The amount of adsorbed BCG on the ADFS, $q_e$ (mg $g^{-1}$), was obtained as follows:

$$q_e = \frac{(C_0 - C_e)}{m} \times V \tag{2}$$

where $q_e$ is the adsorption capacity, $C_0$ and $C_e$ are the initial and equilibrium concentrations of BCG (mg $L^{-1}$), respectively, $m$ is the mass of the adsorbent (g) and $V$ is the solution volume (L).

## Adsorption kinetics

In the present study, three adsorption kinetic models were studied; namely, the Lagergren pseudo-first-order (PFO, eqn (3)),[26,27] pseudo-second-order (PSO, eqn (4))[26,27] and the intraparticle diffusion (IPD, eqn (5)).[27,28]

$$\log(q_e - q_t) = \log q_e - (k_1/2.303)t \tag{3}$$

$$\frac{t}{q_t} = \frac{1}{k_2 {q_e}^2} + \frac{t}{q_e} \tag{4}$$

$$q_t = k_{id} t^{1/2} + I \tag{5}$$

where $q_e$ and $q_t$ are the adsorption capacity (mg $g^{-1}$) at equilibrium and at time $t$, respectively, $t$ is time (min), $k_1$ represents the rate constant of the PFO model (L $min^{-1}$), $k_2$ is the PSO rate constant of adsorption (g $mg^{-1}$ $min^{-1}$), $k_{id}$ is the intraparticle diffusion rate constant (mg $g^{-1}$ $min^{-1/2}$) and $I$ is a constant (mol

$g^{-1}$) that gives information about the thickness of the boundary layer. The larger the $I$ value, the greater is the boundary layer effect.

### Adsorption isotherms

**Freundlich, Langmuir and Temkin isotherms.** Adsorption isotherm models are useful for determining the adsorbate distribution on the surface of the adsorbent at equilibrium conditions. The adsorption isotherm is a plot that describes the adsorption equilibrium at constant temperature and pH.[25] Therefore, the isotherms of Langmuir (eqn (6)),[29,30] Freundlich (nonlinear form eqn (7) and linear form eqn (8))[29,31] and Temkin (eqn (9))[29,32] models were applied in the present study in order to describe the BCG adsorption on the ADFS in aqueous solutions.

$$\frac{C_e}{q_e} = \frac{1}{q_{\max} b} + \frac{1}{q_{\max}} C_e \tag{6}$$

$$\text{Nonlinear form: } q_e = K_F C^{1/n} \tag{7}$$

$$\text{Linear form: } \log q_e = \log K_F + \frac{1}{n} \log C_e \tag{8}$$

$$q_e = \frac{RT}{b_T} \ln A_T + \frac{RT}{b_T} \ln C_e \tag{9}$$

where $C_e$ (mg $L^{-1}$) is the equilibrium or residual concentration of BCG in solution, $q_e$ (mg $g^{-1}$) is the adsorption capacity at equilibrium, $q_{\max}$ (mg $g^{-1}$) is the maximum adsorption capacity, $b$ is the Langmuir constant related to the energy of adsorption (L $mg^{-1}$), $K_F$ is the Freundlich adsorption coefficient related to the adsorption capacity of the adsorbent, *1/n* is a constant that describes the heterogeneity of the adsorbent surface, $R$ is the universal gas constant (8.314 J $K^{-1}$ $mol^{-1}$), $T$ is the absolute temperature in kelvin, $b_T$ is the Temkin isotherm constant related to the heat of adsorption, which indicates the adsorption intensity, and $A_T$ (L $g^{-1}$) is the Temkin isotherm equilibrium binding constant related to the adsorption capacity.

**Scatchard plot.** The Scatchard isotherm (eqn (10)) provides an indication of the nature of the binding sites. The Scatchard plot is a graph of $q_e/C_e$ *versus* $q_e$. Both $K$ (the association constant) and $B_{\max}$ (the maximum number of binding sites) values were determined from the Scatchard linear plot. This method is only valid for a single type of binding sites. Non-linearity or deviation from linearity may indicate the presence of more than one type of binding sites.[33]

$$\frac{q_e}{C_e} = K(B_{\max} - q_e) \tag{10}$$

**Hill plot.** The Hill isotherm model, defined by eqn (11), provides an indication of the nature of the binding sites and describes the homogeneous substrate surface adsorption. This model assumes cooperative monolayer adsorption on different binding sites of the same adsorbent. A plot of $\log(v/(1-v))$ *versus* $\log C$ is used to obtain the values for $K$ and $h$, where $v$ is the saturation fraction, equal to the amount of the bound adsorbate ($q$) divided by the number of binding sites, $q_{\max}$, $C$ is the concentration of the adsorbate BCG, $K$ is the Hill coefficient, $h$, and is an index of cooperativity.[34]

$$\log\left[\frac{v}{1-v}\right] = \log K + h \log C \tag{11}$$

### Adsorption thermodynamics

The thermodynamic studies were carried out in batch conditions using 100 mg $L^{-1}$ BCG solution, an adsorbent dose of 200 mg, 100 min contact time, pH 2, and a temperature range of 303–333 K. The equilibrium constant ($K_F$, Freundlich constant) was calculated from Freundlich equation (eqn (8)). Changes in enthalpy ($\Delta H$) and entropy ($\Delta S$) were determined using van't Hoff's equation (eqn(12)) *via* plotting ln *K*versus*1/T*. Moreover, the Gibb's free energy change ($\Delta G$) was computed using eqn (13).[35,36]

$$\ln K_F = -\frac{\Delta H}{RT} + \frac{\Delta S}{R} \tag{12}$$

$$\Delta G = -RT \ln K_F \tag{13}$$

where $\Delta H$ (kJ $mol^{-1}$) is the enthalpy change, $\Delta S$ (J/molK) is the entropy change, $R$ is the universal gas constant (8.314 J $mol^{-1}$ $K^{-1}$), and $T$ (K) is the absolute temperature.

## Results and discussion

### Characterization of ADFS

In the present work, the ADFS was synthesized *via* diazo-coupling, and the formation of the as-synthesized ADFS was confirmed by several characterization techniques, including FTIR Spectroscopy, XRD, VSM, DLS, FESEM, $^1$H-NMR Spectroscopy, Mass Spectrometry, and Thermal Analyses.

FTIR spectroscopy is a potent characterization tool that may reveal the nature/presence of specific functional groups in a synthesized nanomaterial; consequently, FTIR spectra were recorded to confirm the formation of the ADFS. The infrared absorption spectra of SPIONs, AD, plain ADFS and ADFS with adsorbed BCG were recorded in the spectral window of 4000–400 $cm^{-1}$.

The FTIR spectrum of naked SPIONs (Fig. 2) showed a distinct band at 580 $cm^{-1}$, which corresponds to the stretching of the Fe–O bond. The presence of a carboxylic-metal (Fe–COO) linkage, which may be responsible for the surface negative charges of SPIONs, was confirmed with the sharp absorption band appearing at about 1628 $cm^{-1}$. In addition, the wide absorption band revealed at 3650–3000 $cm^{-1}$ corresponds to O–H stretching vibration in all of the depicted spectra.[37]

The recorded FTIR spectra of ADFS before and after the adsorption of BCG are displayed in Fig. 2. The FTIR spectrum of ADFS before the adsorption of BCG showed an absorption band at 3674 $cm^{-1}$ coming from the stretching vibrations of O–H or N–H, which indicates the ability of ADFS to form hydrogen bonds with BCG molecules. The bands observed at 2989 and

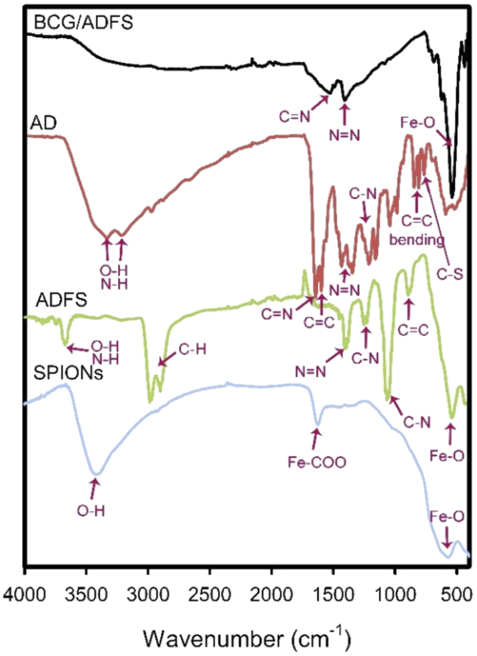

Fig. 2 FTIR spectra of the bare SPIONs, AD, ADFS, and ADFS-BCG.

2905 $cm^{-1}$ stand for the stretching vibrations of C–H. The bands at 1400 and 1382 $cm^{-1}$ are assigned to the asymmetric vibration of –N═N–, indicating that the coupling reaction occurred and the framework of ADFS was successfully formed.[38] The absorption bands appearing at 1240 and 1058 $cm^{-1}$ stand for the stretching vibrations of C–N. Moreover, the bands at 891 and 544 $cm^{-1}$ correspond to –C═C– bond bending and Fe–O bond stretching, respectively.[24,39]

After adsorption of BCG onto the ADFS nanomaterial, the adsorption bands at 1527 and 1406 $cm^{-1}$ are attributed to the stretching vibrations of C═N and N═N, respectively.[40] In addition, the presence of iron (Fe–O bond stretching) was confirmed by the sharp band appearing at 538 $cm^{-1}$. These characteristic bands indicate that BCG was adsorbed onto the ADFS particles.[4,37] Moreover, the disappearance of the absorption band at 3674 $cm^{-1}$ in the spectrum of ADFS confirmed the formation of hydrogen bonds between the hydroxyl and/or amino groups of ADFS and the oxygen atoms of BCG.

The FTIR spectrum of AD (*i.e.* without SPIONs) is displayed in Fig. 2. The C═N and C═C stretching vibrations were observed at 1648 and 1598 $cm^{-1}$, respectively. Furthermore, the bands observed at 1434 and 1345 $cm^{-1}$ were assigned to the asymmetric vibration of –N═N–.[41] The bands that appeared at 1209, 1159, and 1045 $cm^{-1}$ stand for the stretching vibration of C–N. The C═C– bending was detected at 983, 859, and 810 $cm^{-1}$. The stretching vibration of the thiazole ring C–S appeared at 764 $cm^{-1}$.[42,43]

## $^1$H-NMR spectroscopy

The structure of the synthesized thiamine-TBDA azo dye (AD) was verified by $^1$H-NMR spectroscopy. The $^1$H-NMR chemical shifts of the AD are shown in Table 1. The spectrum of the as-synthesized AD shows a singlet peak at 1.1 ppm ($H_e$) corresponding to $CH_3$ protons of TBDA, a multiplet peak at 2–3 ppm attributed to CH and $CH_3$ protons ($H_b$ and $H_d$), a large broad singlet peak at 3.6 ppm assigned to $CH_2$ protons attached to the thiazole ring ($H_i$), a multiplet peak at 4.3 ppm due to $CH_2$ protons ($H_j$), a multiplet peak at 2–3 ppm corresponding to $CH_3$ protons attached to the pyrimidine ring ($H_f$), a singlet peak at 6.08–6.69 ppm attributed to the CH protons of the pyrimidine ring ($H_g$), a doublet peak at 7.2–7.8 ppm attributed to OH proton ($H_a$) and a singlet peak at 8.03 ppm attributed to $CH_3$ protons attached to the thiazole ring ($H_h$). The assignments of the $^1$H-NMR signals are listed in Table 1 and the spectrum is shown in Fig. 3.[44,45]

Table 1 $^1$H-NMR chemical shifts of the thiamine-TBDA azo dye

| Proton symbol | Assignment | $\delta$/ppm | Splitting |
|---|---|---|---|
| a | OH attached to benzene ring | 7.2–7.8 | Doublet |
| b | CH | 2–3 | Multiplet |
| c | OH | 7.2–7.8 | Doublet |
| d | $CH_2$ | 2–3 | Multiplet |
| e | $CH_3$ | 1.065 | Singlet |
| f | $CH_3$ attached to pyrimidine ring | 2–3 | Multiplet |
| g | CH of pyrimidine ring | 6.08–6.69 | Singlet |
| h | $CH_3$ attached to thiazole ring | 8.03 | Singlet |
| i | $CH_2$ attached to thiazole ring | 3.57 | Singlet |
| j | $CH_2$ | 4.3 | Multiplet |

**Mass spectrometry.** Mass spectrometric analysis was used to confirm the thiamine-based AD synthesis by the diazo-coupling reaction shown in Fig. 1A. The molecular ion peak was used to prove the expected chemical structure of the synthesized AD. A molecular ion peak was found at $m/z$ 1038, which matches the expected molecular weight of the prepared AD.

**Thermal analysis.** TGA and DTA thermal analysis techniques were used to study the thermal behaviour of the synthesized AD and ADFS. The analysis was conducted in a nitrogen atmosphere with a temperature range of 25–1000 °C and a heating rate of 10°C $min^{-1}$. The TGA thermogram of the AD (Fig. 4A) shows five decomposition steps, whereas ADFS undergoes four thermal degradation steps (Fig. 4B). Regarding the AD, the first thermal decomposition step, which takes place in the temperature range of 18–148 °C, shows a weight loss of about 3.79%. This weight loss may be attributed to dehydration of the sample. By reaching 1000 °C the total weight loss was 81.76% compared to the original sample weight (*i.e.* almost the whole sample has been decomposed).

The TGA thermogram of the ADFS with its distinctive quadriphasic thermal decomposition pattern is shown in Fig. 4B, where 2.76% of the initial weight was lost at 33–159 °C, which could be attributed to the loss of water molecules.

The total weight loss was found to be 10.49%, indicating the incomplete decomposition of ADFS. These findings confirm the presence of both SPIONs (*i.e.* the thermally stable metal oxide part) and the AD (*i.e.* the relatively thermally unstable organic part).

Fig. 4C and D illustrate DTA profile diagrams of AD and ADFS, respectively. Three exothermic peaks show the oxidative

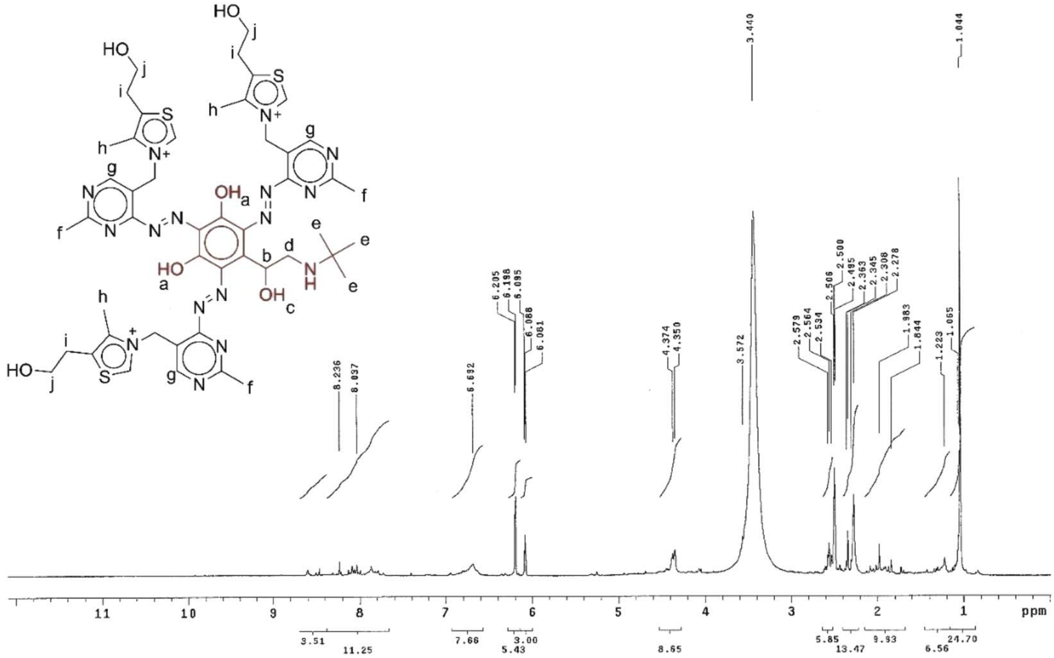

Fig. 3 $^1$H-NMR spectrum of the thiamine-TBDA azo dye in deuterated DMSO.

degradation of the sample on the DTA curve of AD at 159.9, 297.7 and 497.6 °C. Three endothermic peaks illustrating the thermal decomposition of AD were also observed at 750.9, 899.5, and 934.9 °C. On the other hand, the DTA thermogram of ADFS displays two endothermic peaks at 208.3 and 926.9 °C, as well as one exothermic peak at 582.5 °C.

### X-ray diffraction

XRD analysis was used to confirm the crystalline structure of SPIONs. The X-ray diffraction pattern of cubic crystalline magnetite ($Fe_3O_4$, $a = 8.36$ Å) is shown in Fig. 4E. The characteristic peaks at $2\theta$ angles of 30.1, 35.5, 43.2, 53.5, 57.1 and 62.7°

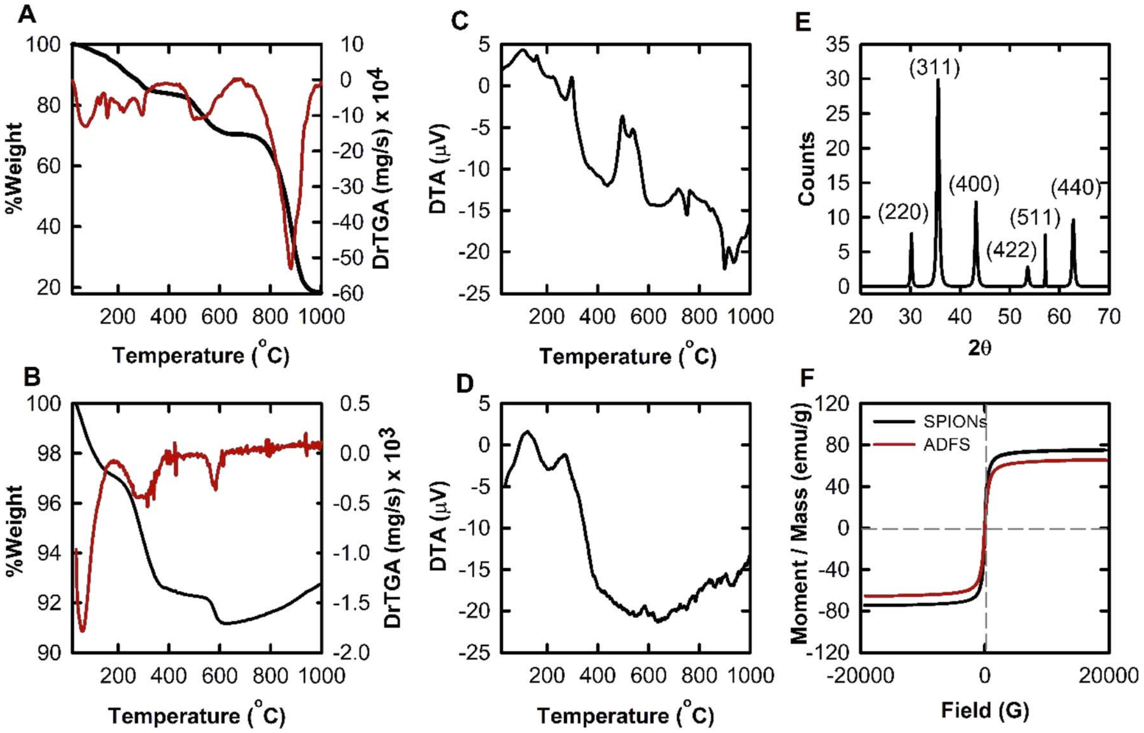

Fig. 4 TGA thermograms and derivative TGA plots of the thiamine-TBDA AD (A) and ADFS (B), DTA thermograms of the thiamine-TBDA AD (C) and ADFS (D), XRD diffractogram of SPIONs (E), and VSM analysis results of the uncoated SPIONs and ADFS (F).

correspond to the (220), (311), (400), (422), (511) and (440) diffraction planes were observed. Meanwhile, these results are in good agreement with those reported in the literature.[46]

### Magnetic susceptibility

The saturation magnetization of SPIONs and ADFS was measured by VSM at room temperature under varying magnetic fields (from −20 to 20 kG), Fig. 4F. The magnetization hysteresis curve shows that both SPIONs and ADFS exhibit superparamagnetic properties because of the high magnetization saturation, low remnant magnetization (3.5 and 5.5 emu $g^{-1}$ for SPIONs and ADFS, respectively) and coercivity (16.5 and 50.6 G, respectively) values. Remnant magnetization is the magnetization left behind in the sample material after removing the external magnetic field. Moreover, coercivity is the resistance of the sample material to variations in magnetization. Coercivity is equivalent to the field intensity necessary to demagnetize the fully magnetized material. The unique soft ferromagnetic properties of the prepared SPIONs arise from their small size.[47–49]

Interestingly, ADFS showed a high magnetization saturation (65.58 emu/g) relative to SPIONs (74.92 emu $g^{-1}$), indicating that the surface coating of SPIONs with AD had no significant effect on their superparamagnetic properties. Therefore, the resulting ADFS can be easily regulated by applying an external magnetic field.

### Dynamic light scattering and zeta potential

The size distribution of SPIONs and ADFS was measured using the dynamic light scattering (DLS) technique in a water suspension at room temperature after ultra-sonication for 15 min in a bath sonicator to avoid particle agglomeration. The obtained results showed that the average particle size of SPIONs and ADFS is about 46.14 and 65.90 nm, respectively. The increase in size indicates the thiamine-TBDA coupling reaction has successfully occurred and the AD was formed around the individual SPIONs.[50]

The surface charge of nanoparticles in a suspension indicates their colloidal stability. SPIONs usually have negative surface charges due to the presence of hydroxyl and carboxylate functional groups (mentioned in the FTIR results). Coating the surface of SPIONs with AD is expected to decrease the number of negative charges on the SPIONs surface; as a result, the apparent ZP will be shifted to a more positive value. The apparent ZP changed from −23.4 mV for SPIONs to −0.56 mV for ADFS, indicating surface coating of SPIONs with the AD.[51]

**Electron microscopy.** SEM imaging was used to visualize the morphology and inner structure of SPIONs and ADFS. Fig. 5 shows the SEM micrographs of SPIONs and ADFS. The microscopic images of SPIONs show small smooth nanoparticles forming agglomerates. As shown in Fig. 5(A and B), the shape of some SPIONs nanoparticles is cubic, indicating the presence of magnetite crystals. However, the morphology of ADFS has changed significantly (Fig. 5C and D). It can be clearly observed that the surface of the ADFS is no longer smooth, which indicates that it has been successfully prepared. Through the thiamine-TBDA coupling reaction, AD was deposited on the surface of SPIONs, which made the ADFS surface rougher compared to bare/uncoated SPIONs.

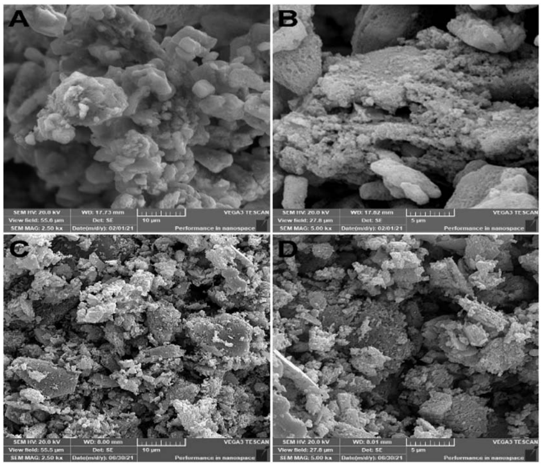

Fig. 5 Scanning electron micrographs of the uncoated SPIONs (A and B) and ADFS (C and D). The magnification power is 2.5 kx in A and C, and 5.0 kx in B and D.

### Effect of solution pH

Both the adsorbent surface and the adsorbate structure in solution can be affected by pH, which is one of the most important environmental parameters. In solutions of different pH, functional groups in the adsorbate and/or adsorbent can be protonated or deprotonated to produce different charges on the adsorbent surface and the adsorbate molecules. This causes electrostatic attraction or repulsion between adsorbate and adsorbent molecules. In addition, the presence of similar electrical charges hinders the formation of hydrogen bonds due to electrostatic repulsion. The absorption spectra of BCG dye in buffer solutions of different pH and their isosbestic point are shown in Fig. 6.[52,53] The effect of pH on BCG removal by ADFS is shown in Fig. 6. The highest removal efficiency was observed at pH 2, and 76% of BCG was removed from the solution by ADFS within 90 min. Then the removal efficiency of BCG decreased dramatically to 39% at pH 4. At higher pH, the removal efficiency continued to decrease until reaching 18%. This variation in the removal efficiency can be explained in terms of the $pK_a$ value of BCG ($pK_a = 4.7$).[38] In addition, the point of zero charge (PZC) of ADFS (pH = 3) was calculated experimentally by adding a constant amount of ADFS solid material to solutions of different pH values (without using a buffer solution) and measuring the final pH of the solution after a certain time of stirring. A plot of ΔpH *versus* the final solution pH can help in determining the PZC.[54,55] Moreover, the solution pH was varied without using a buffer solution, and the final solution pH was measured after adsorption (Fig. 6A). The obtained results coincide with those found by Han *et al.*[54] The measured final solution pH asserts the influence of the electrostatic interactions between the adsorbent and the adsorbate molecules. In a strongly acidic medium (pH < PZC), the ADFS surface bears

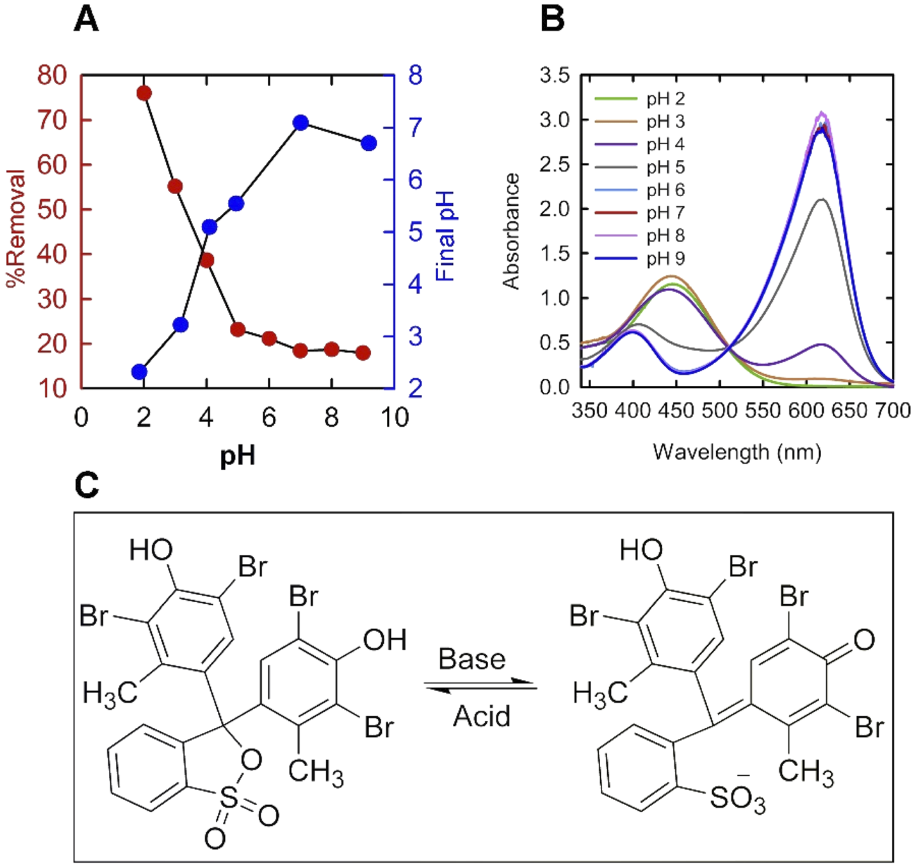

Fig. 6 (A) Effect of pH on the removal percent of BCG from aqueous solution and on the final solution pH, (B) UV-vis spectra of BCG in aqueous solutions of pH 2–9, and (C) the chemical equilibrium between the quinoid and the lactoid forms of BCG in aqueous acidic and alkaline solutions, respectively. The experiments were carried out in triplicates and the obtained standard error values range from 0.45 to 1.26.

a large number of positive charges owing to the presence of protonated amino groups, while BCG molecules are neutral due to the presence of the fully protonated hydroxyl groups. Therefore, the attraction between the electronic cloud (oxygen lone pairs and the π-electrons of the aromatic rings) of BCG and the positive charges on the ADFS surface facilitates the formation of hydrogen bonds between them as described in the FTIR results; thus increasing the removal efficiency. When the final pH is in the range of 3.0 to 4.7, the surface of ADFS is negatively charged and BCG is a neutral molecule, which is not conductive to the formation of hydrogen bonds between them, leading to a decrease in the adsorption efficiency. However, in alkaline solutions (pH > 4.7), the anionic form of BCG molecules is present, while the ADFS surface loses a number of its surface positive charges due to the deprotonation of its terminal as well as internal amino groups. As a result, a repulsive interaction takes place between the anionic BCG molecules and the nitrogen loan pairs of ADFS, thus decreasing the possibility of hydrogen bond formation between them. This leads to a further significant decrease in the removal efficiency. On the other hand, the decrease in final pH after the adsorption of BCG with a high initial pH (pH > 9) is mainly associated with the strong deprotonation on the adsorbent surface (consuming the hydroxyl groups). Therefore, pH 2 was selected as the optimum condition for all the subsequent adsorption experiments. These results coincide with the findings reported by Shokrollahi *et al.*[5]

### Contact time and adsorption kinetics

The effect of the incubation period on the removal efficiency of BCG by ADFS is depicted in Fig. 7A. At an initial concentration of 50 mg $L^{-1}$ of BCG, the removal efficiency rapidly increased by increasing the contact time to 100 min. The adsorption of BCG remained constant after 100 min, implying that equilibrium has been reached. At the beginning, rapid adsorption is observed due to the availability of many free active sites. After a certain time, the adsorption process was hindered as the active sites were gradually occupied. Therefore, an incubation period of 100 min was selected as the optimum contact time for BCG adsorption.[56]

The PFO kinetic model describes the relationship between the adsorption rate and the number of occupied and unoccupied adsorbent sites. Plotting the values of $\log(q_e - q_t)$ against $t$ gives a linear relationship from which $k_1$ and $q_e$ can be calculated from the slope and the intercept, respectively (Fig. 7B). The calculated $q_e$ (0.22 mg $g^{-1}$) is significantly different from the experimental $q_e$ (36.91 mg $g^{-1}$) indicating that the adsorption of BCG onto ADFS does not follow first-order kinetics.[57]

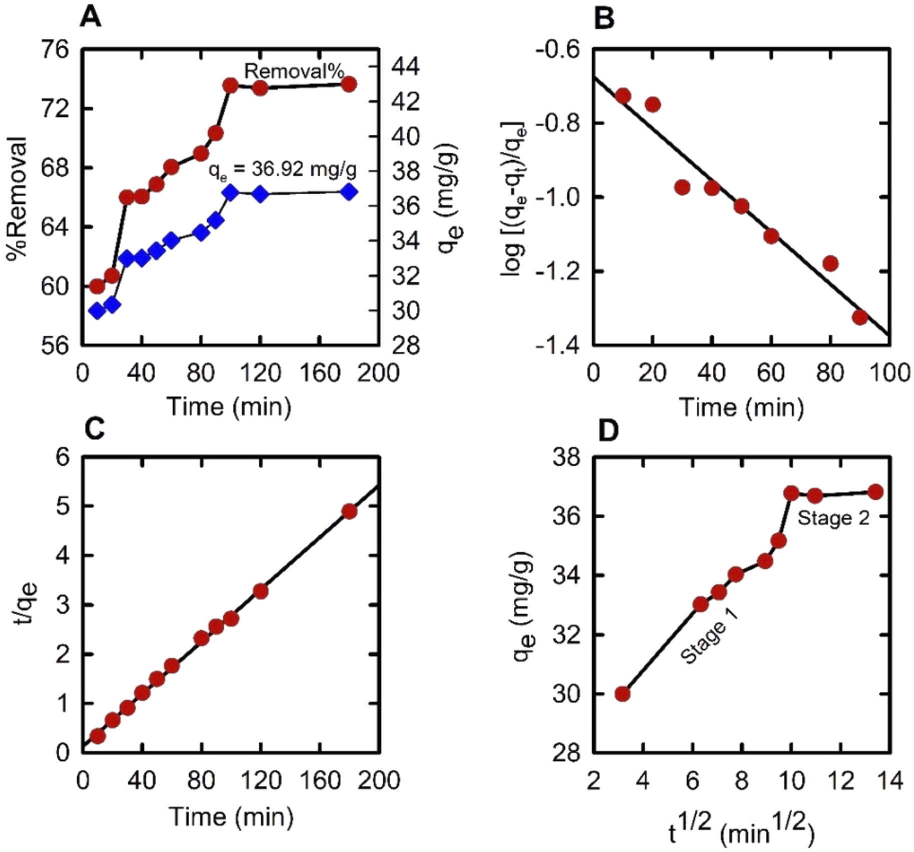

Fig. 7 (A) Influence of time on the removal percent of BCG from aqueous solution, (B) PFO, (C) PSO, and (D) IPD kinetic models for BCG adsorption onto the synthesized ADFS. The experiments were carried out in triplicates and the obtained standard error values range from 0.45 to 1.26.

The PSO kinetic model assumes that the rate of adsorption of a solute is dependent on adsorption capacity, not the adsorbate concentration, and that the rate-limiting step is a chemisorption process. Plotting $t/q_e$ *versus* $t$ gives a linear relationship from which the parameters $k_2$ and $q_e$ can be calculated from the slope and the intercept, respectively (Fig. 7C). The calculated $q_e$ value from the PSO kinetic model was found to be 37.73 mg g$^{-1}$ which is very close to the experimental $q_e$ value (36.91 mg g$^{-1}$). The regression coefficient $r_2$ of the linear plot is 0.9990, which indicates that BCG adsorption on ADFS conforms to second-order kinetics.[58,59]

The IPD kinetic model is shown in Fig. 7D, where the data shows that the adsorption follows a two-stage scenario. Stage 1 is a film-diffusion/rapid-adsorption step that occurs when BCG diffuses through the liquid film that surrounds the ADFS surface, whereas the equilibrium is represented by the plateau at stage 2. The calculated rate constant ($k_{id}$) is 0.79 mg g$^{-1}$ min$^{-1/2}$ and 0.02 mg g$^{-1}$ min$^{-1/2}$ for stage 1 and stage 2, respectively, indicating that the rate of adsorption is faster in the case of the former. Larger intercept values imply a stronger impact of the boundary layer.

The intercept values are 27.67 and 36.52 mg g$^{-1}$ for stage 1 and stage 2, respectively, and the regression coefficient for the linear plots was found to be 0.9082.

### BCG initial concentration and adsorption isotherms

Fig. 8A–C represents the calibration curve of BCG at 444 nm as well as the effect of BCG concentration on the adsorption capacity on the surface of ADFS. When BCG concentration was increased from 10 mg L$^{-1}$ to 100 mg L$^{-1}$, the removal of BCG was reduced from 92.94 to 59.57%, although the adsorption capacity of ADFS increased from 9.29 to 59.57 mg g$^{-1}$. The UV-vis absorption spectra of different concentrations of BCG in aqueous solutions are shown in Fig. 8B.

It has been previously reported that the adsorbent surface contains a fixed number of free active sites per unit mass of the adsorbent. The number of active sites remains high at low initial BCG concentration. At a fixed dose of ADFS and a high concentration of BCG, the available active sites of ADFS become fewer; therefore, some of the BCG molecules cannot be adsorbed and remain in the solution. As the initial concentration is raised, the residual BCG concentration in the solution increases, and consequently, the adsorption effectiveness decreases.[60] In the present work, Langmuir, Freundlich, and Temkin isotherms were used to describe the adsorption of BCG on the surface of the ADFS in aqueous media. The Freundlich model (Fig. 8D) fits the experimental adsorption data better than the Langmuir model. It can be applied for multilayer adsorption to heterogeneous surfaces.[34] Freundlich plot yielded

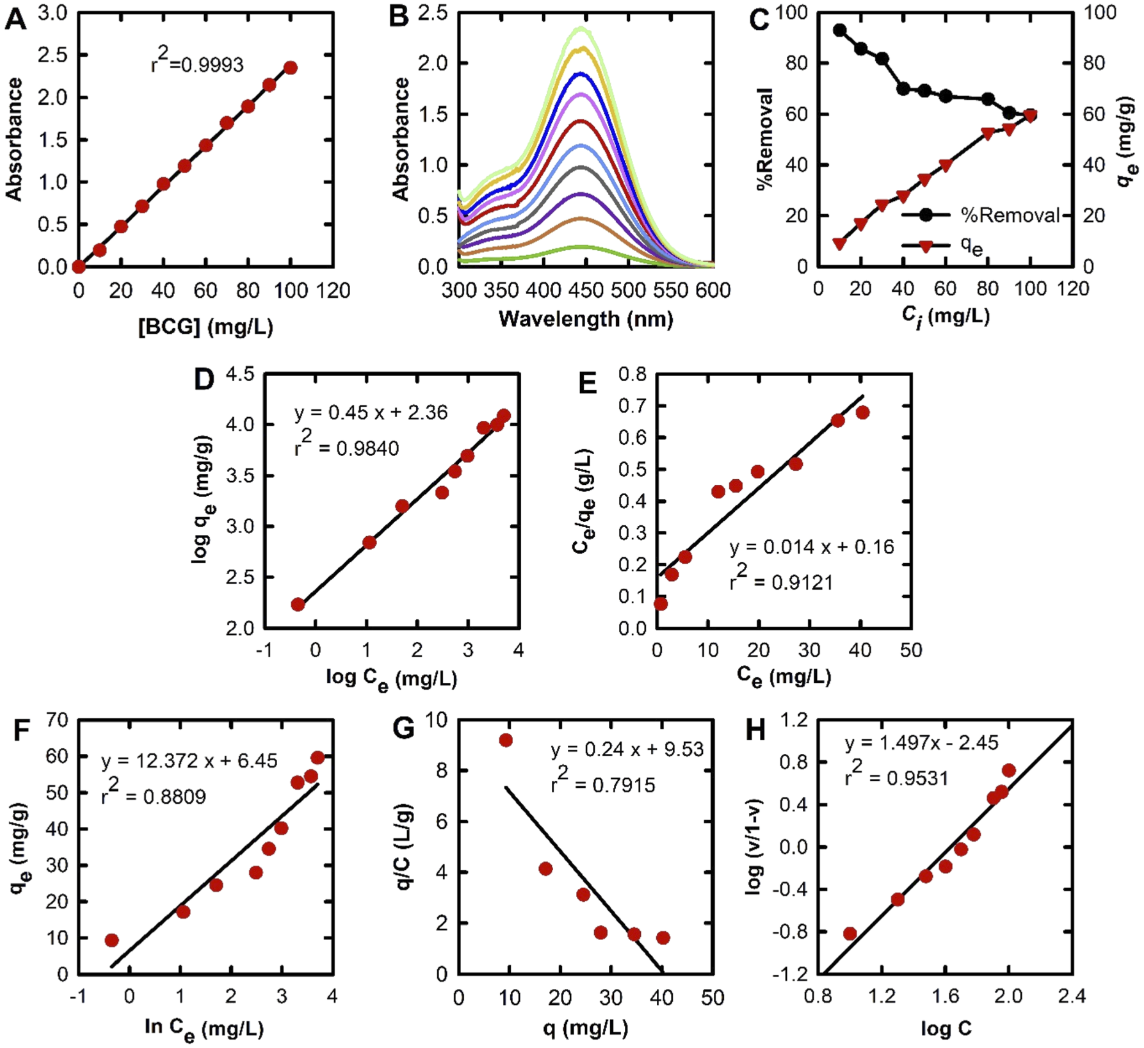

Fig. 8 (A) Standard plot of BCG in aqueous medium, (B) UV-vis spectra of an increasing series of BCG aqueous samples, (C) effect of BCG concentration on the removal percent and equilibrium capacity, (D) Freundlich adsorption isotherm, (E) Langmuir adsorption isotherm, (F) Temkin adsorption isotherm, (G) Scatchard plot, and (H) Hill plot of BCG adsorption onto the synthesized ADFS. The experiments were carried out in triplicates and the obtained standard error values range from 0.45 to 1.26.

a linear correlation coefficient value of 0.9840. The calculated $n$ value indicates whether the adsorption is linear ($n = 1$), favourable physisorption ($2 < n < 10$) or difficult/unfavourable chemisorption ($n < 1$). The calculated $n$ and $K_F$ values are 2.20 and 229.40, respectively, showing that the adsorption process is physisorption and BCG is preferentially adsorbed onto the ADFS surface.[61,62]

The Langmuir isotherm is shown in Fig. 8E and the resulting values of $q_{\max}$, $r^2$ and $b$ were 70.92 mg g$^{-1}$, 0.9121 and 0.09, respectively. The separation factor ($R_L$), defined by eqn (14), can be calculated from Langmuir's model. This value indicates whether the isotherm is irreversible ($R_L = 0$), favourable ($0 < R_L < 1$), linear ($R_L = 1$), or unfavourable ($R_L > 1$). The obtained values of $R_L$ were found to be in the range of 0.10–0.53. The values are less than unity, indicating that the adsorption process is favourable.[63]

$$R_L = \frac{1}{1 + bC_o} \tag{14}$$

where $b$ is Langmuir constant (mg g$^{-1}$) and $C_o$ is initial concentration of adsorbate (mg L$^{-1}$).

The heat of adsorption was also calculated using the Temkin isotherm (Fig. 8F). In Temkin isotherm, it is assumed that the heat of adsorption of all molecules in the layer decreases as the surface coverage increases. The constants $b_T$ and $A_T$ can be calculated from the slope and intercept, respectively, by graphing ln $C_e$ *versus* $q_e$. When the $b_T$ value is less than $8 \times 10^4$, the adsorption is considered a physisorption process. However, heat of adsorption ($B = RT/b_T$) provides information on the strength of interaction between the adsorbent and the adsorbate. When the value of $B$ is less than 8 kJ mol$^{-1}$, it implies that the adsorbate molecules have a weak interaction with the adsorbent surface. The obtained $b_T$ value is about 200.26 whereas the $B$ value is 12.37 J mol$^{-1}$ and the correlation coefficient of the Temkin plot is 0.8809, indicating that the adsorption process is physisorption.[62–64] Based on the regression correlation coefficient values of the three isotherms, the

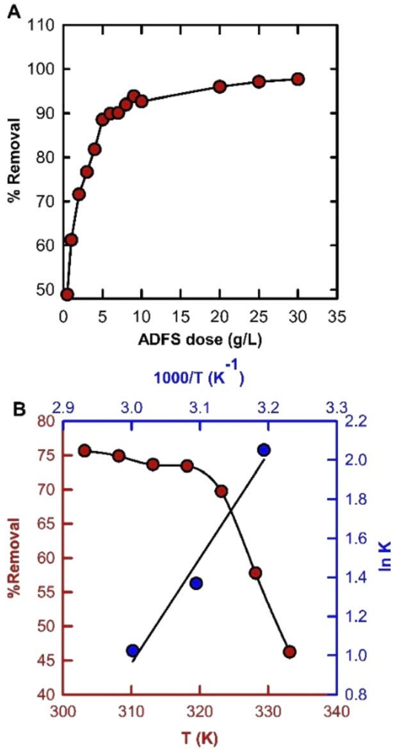

Fig. 9 (A) The influence of ADFS dose, and (B) thermodynamics and the effect of aqueous solution temperature on the adsorption of BCG onto the synthesized ADFS adsorbent. The experiments were carried out in triplicates and the obtained standard error values range from 0.45 to 1.26.

Table 2 Thermodynamic parameters of BCG adsorption on ADFS

| $\Delta H$ (kJ mol$^{-1}$) | $\Delta S$ (kJ mol$^{-1}$ K$^{-1}$) | $\Delta G$ (kJ mol$^{-1}$) | | |
|---|---|---|---|---|
| | | 313 K | 323 K | 333 K |
| −44.70 | −0.13 | −5.34 | −3.68 | −2.83 |

Freundlich isotherm model is the best model that describes the adsorption of BCG onto the ADFS surface. According to the Freundlich model, the adsorption is a physisorption process. Therefore, the interactions between BCG and ADFS are governed by weak intermolecular forces rather than covalent bonding. Despite the fact that the Freundlich model was selected as the best, the other isotherms reached the same conclusion.

In the current study, Scatchard analysis and Hill plots were used to understand the interaction of the adsorbent with the adsorbate and to determine the number of binding sites on the adsorbent surface. Scatchard plots with a negative slope give positive values of the association constant (*K*). The calculated *K* from Scatchard analysis is 0.23 g L$^{-1}$ (Fig. 8G). The presence of nonspecific binding or multiple classes of binding sites for BCG adsorption could explain a concave upward Scatchard plot like the one reported in this study.[65]

The Hill plot is shown in Fig. 8H, and the resulting value of the cooperativity index (*h*) was found to be 1.50 (larger than unity), indicating that the ADFS has multiple binding sites with positive cooperativity. This finding is consistent with the results obtained from the Scatchard analysis in the previous section.[15]

### ADFS dose

The effect of the adsorbent dose on the removal efficiency of BCG is depicted in Fig. 9A. The removal efficiency increased from 48.89 to 97.68% upon increasing the ADFS dose from 5 to 300 mg, owing to the availability of new active sites for BCG adsorption.[66]

### Adsorption thermodynamics and the effect of temperature

Temperature is a significant factor that can affect BCG adsorption behaviour on the ADFS surface (Fig. 9B). The maximum removal efficiency was achieved at room temperature, making the synthesized ADFS a promising material for removing BCG from contaminated water. The adsorption thermodynamic parameters ($\Delta G$, $\Delta H$, and $\Delta S$) were calculated, and then the spontaneity and heat change of the adsorption process could be investigated (Table 2). The adsorption of BCG onto ADFS was found to be a spontaneous process due to the obtained negative values of $\Delta G$ at the studied temperatures. The calculated $\Delta G$ values could imply that the type of adsorption is either physisorption ($-20 < \Delta G < 0$ kJ mol$^{-1}$) or chemisorption ($-400 < \Delta G < -80$ kJ mol$^{-1}$). In the studied temperature range, $\Delta G$ for BCG adsorption was in the range from −2.83 to −5.34 kJ mol$^{-1}$, indicating that the adsorption occurs *via* a physisorption process. The negative values of $\Delta G$ imply that BCG adsorption on ADFS is a spontaneous process and that the adsorbate prefers to remain in the stationary/adsorbed phase rather than in the solution phase.[67,68] These results coincide with those of the adsorption isotherms.

The four fundamental noncovalent interactions are electrostatic, hydrophobic, van der Waals, and hydrogen bonding. The values of $\Delta$H and $\Delta S$ can be used to predict the type of interaction between the adsorbent and the adsorbate. Hydrophobic interactions can be dominated by either enthalpy-driven processes such as hydrogen bonding and van der Waals interactions ($\Delta S < 0$, $\Delta H < 0$ and $|\Delta H| > |T\Delta S|$) or entropy-driven processes ($\Delta S > 0$, $\Delta H > 0$ and $|\Delta H| < |T\Delta S|$). Electrostatic interactions are characterized by a positive value of $\Delta S$ and a minor value of $\Delta H$ ($\Delta S > 0$ and $\Delta H \sim 0$). The adsorption of BCG on ADFS was found to be enthalpy-driven by hydrogen bonding and van der Waals interactions (Table 2).[68]

## Conclusions

In this work, we designed a novel, highly efficient adsorbent superparamagnetic nanomaterial for the removal of a model anionic dye, BCG, from water. The materials used to manufacture the proposed adsorbent are environmentally friendly, as they are composed of the product of a diazo–coupling reaction between vitamin B1 (thiamine) and another pharmaceutical molecule (TBDA), along with biocompatible superparamagnetic iron oxide nanoparticles. The synthesis methodology is straightforward and easily scalable. In addition, reproducible results were obtained upon repeating the same synthesis protocol. The applied superparamagnetic adsorbent nanomaterial showed excellent BCG removal efficiency at room temperature. Physicochemical characterization of the proposed adsorbent revealed a very large surface area due to its small particle size. In addition, it has the advantage of being easily removed from water after treatment by applying a strong external magnetic field. Therefore, the proposed adsorbent nanomaterial could be applied to remove anionic contaminants from water. Additional research is still needed to investigate the possibility of using other amines and coupling agents to prepare similar high-molecular-weight azo dye-based adsorbents to remove neutral, anionic, or cationic water pollutants.

## Author contributions

Hadeel Saad: methodology, investigation, formal analysis, visualization, data curation, resources, writing-original draft. F. A. Nour El-Dien: supervision, project administration, resources, writing-review and editing. Nadia E. A. El-Gamel: supervision, writing-review and editing. Ahmed S. Abo Dena: conceptualization, methodology, investigation, resources, formal analysis, data curation, visualization, writing-review and editing.

## Conflicts of interest

There are no conflicts to declare.

## Notes and references

1 E. F. D. Januário, T. B. Vidovix, N. de C. L. Beluci, R. M. Paixão, L. H. B. R. da Silva, N. C. Homem, R. Bergamasco and A. M. S. Vieira, *Sci. Total Environ.*, 2021, **789**, 147957.
2 B. Lellis, C. Z. Fávaro-Polonio, J. A. Pamphile and J. C. Polonio, *Biotechnol. Res. Innov.*, 2019, **3**, 275–290.
3 A. S. Shair, A. S. Abo Dena and I. M. El-Sherbiny, *Spectrochim. Acta, Part A*, 2021, **249**, 119301.
4 A. S. Abo Dena and W. M. I. Hassan, *Spectrochim. Acta, Part A*, 2016, **163**, 108–114.
5 A. Shokrollahi, A. Alizadeh, Z. Malekhosseini and M. Ranjbar, *J. Chem. Eng. Data*, 2011, **56**, 3738–3746.
6 T. J. Kindala, S. J. Kayembe, K. A. Kifuani, L. B. Ilinga and K. M. Taba, *J. en Ligne l'ACASTI du CEDESURK*, 2015, **3**, 67–74.
7 E. Salmalian, H. Rezaei and A. A. Shahbazi, 2019.
8 Y. Lu, B. Wei, Y. Wang and J. Li, *Sep. Sci. Technol.*, 2007, **42**, 1901–1911.
9 G. Matyszczak, K. Krzyczkowska and K. Krawczyk, *Water Sci. Technol.*, 2021, **84**, 3227–3236.
10 L. Chen, L. Wu, F. Liu, X. Qi, Y. Ge and S. Shen, *J. Mater. Chem. B*, 2016, **4**, 3660–3669.
11 S. Laurent, A. A. Saei, S. Behzadi, A. Panahifar and M. Mahmoudi, *Expert Opin. Drug Deliv.*, 2014, **11**, 1449–1470.
12 O. A. Abdel Aziz, K. Arafa, A. S. Abo Dena and I. M. El-sherbiny, *J. Nanotechnol. Adv. Mater.*, 2020, **8**, 21–29.
13 N. A. Wibowo, H. Sabarman and E. Suharyadi, *Adv. Nat. Sci. Nanosci. Nanotechnol.*, 2021, **12**, 45013.
14 C. Pandit, H. K. Alajangi, J. Singh, A. Khajuria, A. Sharma, M. S. Hassan, M. Parida, A. D. Semwal, N. Gopalan, R. K. Sharma, A. Suttee, U. Soni, B. Singh, S. Sapra, R. P. Barnwal, G. Singh and I. P. Kaur, *Sci. Total Environ.*, 2022, **831**, 154857.
15 H. Saad, F. A. Nour El-Dien, N. E. A. El-Gamel and A. S. Abo Dena, *RSC Adv.*, 2021, **11**, 39768–39780.
16 Y. Nie, Y. Luo, S. Luo, X. Cao, G. Song and C. Deng, *J. Chromatogr. A*, 2022, **1662**, 462733.
17 K. Banan, F. Ghorbani-Bidkorbeh, H. Afsharara, D. Hatamabadi, B. Landi, R. Keçili and B. Sellergren, *Anal. Chim. Acta*, 2022, **1198**, 339548.
18 A. S. Abo Dena and I. M. El-Sherbiny, ed. M. S. Hasnain, S. Beg and A. K. B. T.-C. in B. A. Nayak, *Bioimaging applications of chitosan-based systems*, Academic Press, 2022, pp. 383–395.
19 A. Yadav, C. Rao, K. Kaushik, F. Anjum, S. Sharma and C. K. Nandi, *ACS Appl. Nano Mater.*, 2022, **5**, 4018–4027.
20 S. Benkhaya, S. M'rabet and A. El Harfi, *Heliyon*, 2020, **6**, 1.
21 S. B. Patel and D. V Vasava, *Nano-Structures & Nano-Objects*, 2020, **21**, 100416.
22 O. Sadak, R. Hackney, A. K. Sundramoorthy, G. Yilmaz and S. Gunasekaran, *Environ. Nanotechnol. Monit. Manag.*, 2020, **14**, 100380.
23 R. Mahajan, S. Suriyanarayanan and I. A. Nicholls, *Nanomaterials*, 2021, **11**(8), 1–13.
24 Y. Shen, W.-X. Ni and B. Li, *ACS Omega*, 2021, **6**, 3202–3208.
25 B. O. Isiuku, P. C. Okonkwo and C. D. Emeagwara, *J. Dispers. Sci. Technol.*, 2021, **42**, 1879–1897.
26 S. Hussain, M. Kamran, S. A. Khan, K. Shaheen, Z. Shah, H. Suo, Q. Khan, A. B. Shah, W. U. Rehman, Y. O. Al-Ghamdi and U. Ghani, *Int. J. Biol. Macromol.*, 2021, **168**, 383–394.
27 C. Marcu, C. Varodi and A. Balla, *Anal. Lett.*, 2021, **54**, 140–149.
28 Z. Fang, H. Suhua, L. Xu, F. Jian, L. Qi, W. Zhiwei, L. Chuanchang and X. Yuanlai, *Colloids Surfaces A Physicochem. Eng. Asp.*, 2021, **627**, 127063.
29 G. K. Rajahmundry, C. Garlapati, P. S. Kumar, R. S. Alwi and D.-V. N. Vo, *Chemosphere*, 2021, **276**, 130176.
30 F. Karimi, A. Ayati, B. Tanhaei, A. L. Sanati, S. Afshar, A. Kardan, Z. Dabirifar and C. Karaman, *Environ. Res.*, 2022, **203**, 111753.
31 M. Hamzaoui, B. Benaouda and N. Benderdouche, *J. Mater. Environ. Sci.*, 2018, **9**(4), 1110–1118.
32 S. A. Al-Trawneh, A. G. Jiries, S. F. Alshahateet and S. Sagadevan, *Chem. Phys. Lett.*, 2021, **781**, 138959.
33 L. C. Overah, *Nigerian Journal of Science and Environment*, 2021, **19**, 1.
34 N. Ayawei, A. N. Ebelegi and D. Wankasi, *J. Chem.*, 2017, **2017**, 3039817.
35 N. Boukhalfa, M. Boutahala, N. Djebri and A. Idris, *Int. J. Biol. Macromol.*, 2019, **123**, 539–548.
36 F. Batool, J. Akbar, S. Iqbal, S. Noreen and S. N. A. Bukhari, *Bioinorg. Chem. Appl.*, 2018, **2018**, 3463724.

37 L. F. Peffi Ferreira, T. de Oliveira, S. H. Toma, M. M. Toyama, K. Araki and L. H. Avanzi, *RSC Adv.*, 2020, **10**, 38490–38496.

38 D. Liu, J. Yuan, J. Li and G. Zhang, *ACS Omega*, 2019, **4**, 12680–12686.

39 J. Zhuang, M. Li, Y. Pu, A. J. Ragauskas and C. G. Yoo, *Appl. Sci.*, 2020, **10**(12), 1–13.

40 N. B. Colthup, L. H. Daly and S. E. Wiberley, *Introduction to Infrared and Raman Spectroscopy*, Academic Press, San Diego, 3rd edn, 1990, pp. 261–288.

41 D. Jiang, R. Deng, G. Li, G. Zheng and H. Guo, *RSC Adv.*, 2020, **10**, 6185–6191.

42 O. E. Sherif, Y. M. Issa and A. S. A. Dena, *Int. J. Adv. Res.*, 2015, **3**, 969–976.

43 S. M. El-Megharbel, R. Z. Hamza, A. A. Gobouri and M. S. Refat, *Appl. Organomet. Chem.*, 2019, **33**, e4892.

44 E. Varga, G. Benkovics, A. Darcsi, B. Várnai, T. Sohajda, M. Malanga and S. Béni, *Electrophoresis*, 2019, **40**, 2789–2798.

45 A. Igoshi, K. Noda and M. Murata, *Biosci. Biotechnol. Biochem.*, 2018, **82**, 1425–1432.

46 A. Kumar, G. Sharma, M. Naushad and S. Thakur, *Chem. Eng. J.*, 2015, **280**, 175–187.

47 S. Prijic, J. Ščančar, R. Romih, M. Cemazar, V. Bregar, A. Znidarsic and G. Sersa, *J. Membr. Biol.*, 2010, **236**, 167–179.

48 X. He, W. Zhong, C.-T. Au and Y. Du, *Nanoscale Res. Lett.*, 2013, **8**, 446.

49 B. Liu, H. Liu, W. Li, Y. Li, Y. Lan and Y. Li, *Environ. Sci. Water Res. Technol.*, 2021, **7**, 1985–1995.

50 A. Samui, N. Kesharwani, C. Haldar and S. K. Sahu, *Microporous Mesoporous Mater.*, 2020, **299**, 110112.

51 C. C. Hanot, Y. S. Choi, T. B. Anani, D. Soundarrajan and A. E. David, *Int. J. Mol. Sci.*, 2016, **17**(1), 1–15.

52 S. Iftekhar, D. L. Ramasamy, V. Srivastava, M. B. Asif and M. Sillanpää, *Chemosphere*, 2018, **204**, 413–430.

53 Z. Wu, X. Ye, H. Liu, H. Zhang, Z. Liu, M. Guo, Q. Li and J. Li, *Pure Appl. Chem.*, 2020, **92**(10), 1655–1662.

54 Y. Han, C. Chen, Y. Li, L. Zhou, Y. Lan and Y. Li, *Sep. Purif. Technol.*, 2019, **213**, 410–418.

55 Y. Li, Y. Han, W. Li, Y. Li, D. Zhang and Y. Lan, *Environ. Res.*, 2020, **180**, 108896.

56 S. K. Ponnusamy, C. Vincent, K. Kirthika and K. Kumar, *Brazilian J. Chem. Eng.*, 2010, **27**(2), 339–346.

57 U. A. Edet and A. O. Ifelebuegu, *Processes*, 2020, **8**, 665–679.

58 M. Haghighi and A. Khoshfetrat, *Int. J. Chem. Eng.*, 2021, **2021**, 2040363.

59 D. Robati, *J. Nanostructure Chem.*, 2013, **3**, 55.

60 U. Pathak, P. Das, P. Banerjee and S. Datta, *J. Thermodyn.*, 2016, **2016**, 3746316.

61 A. R. Kul and N. Caliskan, *Adsorpt. Sci. Technol.*, 2009, **27**, 85–105.

62 T. Z. E. Lee, J. Zhang, Y. Feng, X. Lin and J. Zhou, *IOP Conf. Ser. Earth Environ. Sci.*, 2021, **657**, 12026.

63 B. Meroufel, B. Omar, B. Mohamed, Y. Benmoussa and M. A. Zenasni, *J. Mater. Environ. Sci.*, 2013, **4**, 482–491.

64 F. Togue Kamga, *Appl. Water Sci.*, 2018, **9**, 1.

65 K. Wilkinson, *Methods Mol. Biol.*, 2004, **261**, 15–32.

66 T. Sarwar, F. Memon, A. Memon, F. Durmaz, S. Memon, D. Panhwar and S. Muneer, *Sep. Sci. Technol.*, 2018, **54**, 1–11.

67 C. Wu, X. Lou, A. Huang, M. Zhang and L. Ma, *Appl. Clay Sci.*, 2020, **190**, 105566.

68 C. Wu, X. Lou, X. Xu, A. Huang, M. Zhang and L. Ma, *ACS Omega*, 2020, **5**, 4191–4199.